Letters in Applied NanoBioScience
Open-Access Journal (ISSN: 2284-6808)

Article
Volume 15, Issue 2, 2026, 69
https://doi.org/10.33263/LIANBS152.069

Entropy Generation in Hybrid Nanofluid Flow Over a Stretching Sheet with First-Order Slip, Suction/Injection, and Chemical Reaction

Prasanta Parida [1], Hibah Islahi [2], Kharabela Swain [3,*]

[1] Research Scholar, Institute of Applied Sciences, Mangalayatan University, Aligarh-202146, India
[2] Institute of Applied Sciences, Mangalayatan University, Aligarh-202146, India
[3] Department of Mathematics, GIFT Autonomous, Bhubaneswar-752054, India
* Correspondence: kharabelaswain@gift.edu.in;

Received: 11.05.2025; Accepted: 21.02.2026; Published: 30.06.2026

Abstract: The first-order slip boundary condition finds wide application in micro- and nanoscale fluid systems where the conventional no-slip assumption breaks down. It is particularly relevant in modeling nanofluid transport, microchannel heat exchangers, and rarefied gas dynamics, enabling more accurate predictions of flow and heat transfer behavior at small scales. Entropy generation analysis in nanofluid flow and heat transfer provides a framework to minimize irreversibilities and optimize thermal system efficiency, particularly in microchannel and energy applications. This research investigates the influence of first-order velocity slip and injection/suction effects on the steady 2-D flow of hybrid nanofluid (HNF) over a linearly stretching sheet embedded in a porous medium with entropy generation and nth order chemical reaction. The HNF is modeled by a combination of Single-Walled Carbon Nanotubes ($SWCNT$), Multi-Walled Carbon Nanotubes ($MWCNT$) as nanoparticles (NPs) with water as base fluid to enhance thermal conductivity and overall heat transfer performance. By applying similarity transformations, the governing PDEs are reduced to a system of ODEs and then solved numerically using the bvp4c solver in MATLAB 2024a. The effects of the relevant physical parameters on flow, heat transfer, and mass transfer are analyzed and discussed quantitatively. Results reveal that the effect of injection is to decrease both heat and mass transfer coefficients at the bounding surface, resulting in cooling of the plate with low mass flux, but the suction does the reverse. Decrease in porosity parameter (Kp) from 100 to 1 gives rise to a decrease in skin friction coefficient (C_f) 61.57% and the Nusselt number increases by about 0.21%, while the Sherwood number increases by nearly 0.20%, indicating marginal improvements in heat and mass transfer, respectively.

Keywords: entropy generation; stretching sheet; suction/injection; viscous dissipation; joule heating; chemical reaction.

1. Introduction

The analysis of HNF flow over stretching surfaces under slip conditions has received significant attention due to its relevance in modern microfluidic, thermal, and biomedical engineering applications. The classical stretching sheet problem, first introduced by Sakiadis [1] and later extended by Crane [2], laid the foundation for boundary-layer studies in manufacturing processes such as extrusion and polymer sheet drawing. With the introduction

of NFs by Choi [3] and further theoretical advancements by Buongiorno [4], researchers initiated incorporating NPs into base fluids to enhance thermal conductivity and energy transport. Nadeem *et al*. [5] and Mustafa *et al*. [6] investigated the effect of nanofluid flow past a stretching sheet.

Slip boundary conditions are widely employed in fluid dynamics to account for velocity deviations at the fluid–solid interface, particularly at micro- and nanoscales where the classical no-slip assumption (velocity of the fluid at the wall equals the wall velocity) becomes invalid. This condition becomes important when the mean free path of fluid particles is comparable to the characteristic length scale of the flow (high Knudsen number regimes). They are crucial in modeling flows in microchannels, nanochannels, and porous media, as well as in nanofluid transport and thermal management systems. More recently, Rao and Deka [7] studied HNF $(Ag - Al_2O_3/water)$ flow over a stretching sheet with first-order boundary slip conditions. Suction and injection mechanisms are well known to control boundary layer thickness and stability. Suction stabilizes the flow by thinning the boundary layer, thereby enhancing heat and mass transfer [8]. On the other hand, injection introduces instabilities and increases boundary layer thickness, which can be utilized in controlled drug delivery and chemical coating applications.

Entropy generation analysis is widely applied in optimizing thermal and fluid systems by identifying sources of irreversibility. It is particularly useful in the design of heat exchangers, microscale cooling devices, and energy systems, where minimizing entropy production enhances performance and efficiency. In nanofluid flow and microscale transport, it provides insight into the trade-off between heat transfer enhancement and additional irreversibilities, supporting the development of more efficient thermal management technologies. Recent studies have explored diverse areas, including nanofluids, magnetohydrodynamic (MHD) flows, porous media, renewable energy systems, and electronic component analysis. Zahor *et al*. [9] conducted a comprehensive review focusing on mathematical models for entropy generation in MHD flows of NFs through porous media. They analyzed how parameters such as velocity and temperature profiles influence entropy generation. Their work aims to identify research gaps and propose future research in this domain. Elhaj *et al*. [10] studied entropy generation minimization in two-phase flow irreversibilities within hydrocarbon reservoirs. They developed predictive models to calculate energy losses in porous media and wellbores, considering factors such as temperature, wettability, and capillary pressure.

Khan and Pop [11] employed Buongiorno's model to examine the effects of thermophoresis and Brownian motion of nanoparticles. These are the two primary mechanisms governing NP diffusion in NFs. Thermophoresis (the motion of particles from hot to cold regions) has a greater impact on the concentration profile than Brownian motion, leading to a higher accumulation of NPs near the surface. Swain *et al*. [12] presented a numerical study on the 2-D flow of a Cu-water NF over a stretching/shrinking sheet. The results revealed that increasing the inclination angle of the magnetic field reduces fluid velocity and increases the thermal boundary layer thickness, indicating enhanced resistive effects. Joule heating was found to significantly raise the fluid temperature due to energy dissipation from electrical conductivity. These findings have potential implications in industrial processes involving heat transfer enhancement using NFs under magnetic and thermal control. Al-Kouz *et al*. [13] found that an exponential heat source raised the temperature profile, thereby intensifying the thermal boundary layer thickness. Further, hybrid NF showed better thermal conductivity than mono

NF, resulting in more efficient heat transfer. Swain *et al*. [14] revealed that the inclusion of MWCNT/Fe_3O_4 hybrid NPs significantly enhanced thermal conductivity and improved heat transfer performance compared to single-component NFs. Waini *et al*. [15] and Devi. [16] showed that the HNF has better heat transfer rates compared to NFs due to the high thermal properties of the NPs. Ahmad *et al*. [17] examined that both the temperature and concentration profiles are strongly influenced by the NP volume fraction and thermal diffusion, making these key design parameters for practical thermal systems. Several authors [18-36] have investigated the MHD flow of nanofluid and hybrid nanofluid using different flow geometries.

The novelty of this study lies in the combined effects of first-order slip, suction/injection, and nth-order chemical reaction on entropy generation in hybrid nanofluid (MWCNT–SWCNT/water) flow over a stretching sheet embedded in a porous medium. Previous studies have not addressed hybrid nanofluid flow in a porous medium under the simultaneous effects of entropy generation and chemical reaction, an approach that provides a more comprehensive understanding of transport irreversibility. The use of a hybrid carbon-based nanofluid enhances thermal conductivity beyond that of conventional monofluids, offering improved heat transfer. Furthermore, incorporating Bejan number analysis provides insights into the relative dominance of heat, viscous, and mass-transfer irreversibilities, which have not been extensively reported for CNT-based hybrid nanofluids. These aspects make the present investigation distinct and relevant for advanced energy, thermal management, and microfluidic applications.

2. Design of the Problem

Consider the steady, two-dimensional, laminar, and incompressible flow of HNF over a stretching sheet. The study comprises $SWCNT$, and $MWCNT$ as nanoparticles with water (H_2O) as regular fluid, the sheet is placed in the direction of the *x*-axis, and the *y*-axis is normal to the sheet. A constant magnetic field strength B_0 is applied in the direction of the *y*-axis. The sheet is stretched with the velocity $u_w(x) = ax$ where $a > 0$ is constant, and the constant mass flux velocity is denoted by $v_0 = -\sqrt{av_f}S$ where S is a constant. The surface and ambient temperatures and concentrations are, respectively T_w, T_∞ and C_w, C_∞. This model takes care of the cross flow, i.e., suction/injection at the bounding surface. The flow geometry of the present model is exhibited in Figure 1.

Assumptions of the present model: The flow is steady, two-dimensional, laminar, and incompressible. The base fluid is water, and the hybrid nanofluid (HNF) is formed by suspending SWCNT and MWCNT nanoparticles. Nanoparticles are uniformly dispersed in the base fluid with no agglomeration or sedimentation. A constant magnetic field is applied perpendicular to the sheet. The fluid is electrically conducting, so magnetic (Lorentz) force and Joule heating effects are considered. The porous medium is homogeneous and isotropic, characterized by a porosity parameter. The surface temperature and concentration are kept constant, different from ambient conditions. The model incorporates a first-order slip boundary condition at the wall (velocity slip). The chemical reaction is assumed to be a homogeneous single-step nth-order process affecting only the concentration field, with constructive or destructive effects represented by the reaction parameter. Entropy generation arises from heat transfer, mass diffusion, viscous dissipation, and Joule heating, while radiation effects are neglected, and the Bejan number is used to assess irreversibility contributions.

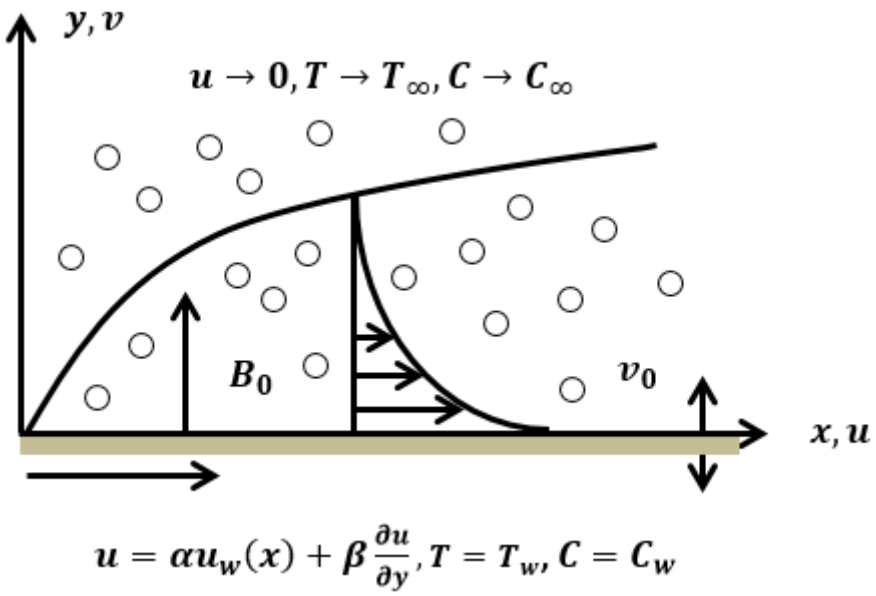

Figure 1. Flow geometry of the problem.

The governing equations following [16,17] are given by:

$$\frac{\partial u}{\partial x}+\frac{\partial v}{\partial y}=0 \tag{1}$$

$$u\frac{\partial u}{\partial x}+v\frac{\partial u}{\partial y}=\frac{\mu_{hnf}}{\rho_{hnf}}\frac{\partial^2 u}{\partial y^2}-\frac{\sigma_{hnf}}{\rho_{hnf}}B_0^2u+\frac{\mu_{hnf}}{Kp^*\rho_{hnf}}u \tag{2}$$

$$u\frac{\partial T}{\partial x}+v\frac{\partial T}{\partial y}=\frac{k_{hnf}}{(\rho C_p)_{hnf}}\frac{\partial^2 T}{\partial y^2}+\frac{\sigma_{hnf}}{(\rho C_p)_{hnf}}B_0^2u^2+\frac{\mu_{hnf}}{(\rho C_p)_{hnf}}\left(\frac{\partial u}{\partial y}\right)^2 \tag{3}$$

$$u\frac{\partial C}{\partial x}+v\frac{\partial C}{\partial y}=D_B\frac{\partial^2 C}{\partial y^2}-Kc^*(C-C_\infty)^n \tag{4}$$

$$\left.\begin{array}{c} u=\alpha u_w(x)+\beta\frac{\partial u}{\partial y}, v=v_0, T=T_w, C=C_w \ at\ y=0 \\ u\to 0, T\to T_\infty, C\to C_\infty \ as\ y\to\infty \end{array}\right\} \tag{5}$$

Consider the following dimensionless variables:

$\psi=\sqrt{av_f}xf(\eta), \eta=y\sqrt{a/v_f}, \theta=\frac{T-T_\infty}{T_w-T_\infty}, \Phi=\frac{C-C_\infty}{C_w-C_\infty}, u=axf'(\eta)$ and $v=-\left(\sqrt{av_f}\right)f(\eta)$ we get:

$$\frac{\mu_{hnf}/\mu_f}{\rho_{hnf}/\rho_f}f'''+ff''-f'^2-\frac{\sigma_{hnf}/\sigma_f}{\rho_{hnf}/\rho_f}Mf'-\frac{\mu_{hnf}/\mu_f}{\rho_{hnf}/\rho_f}\frac{f'}{Kp}=0 \tag{6}$$

$$\frac{1}{Pr}\frac{1}{(\rho C_p)_{hnf}/(\rho C_p)_f}\frac{k_{hnf}}{k_f}\theta''+f\theta'+\frac{\sigma_{hnf}/\sigma_f}{(\rho C_p)_{hnf}/(\rho C_p)_f}MEcf'^2+\frac{\mu_{hnf}/\mu_f}{(\rho C_p)_{hnf}/(\rho C_p)_f}Ecf''^2=0 \tag{7}$$

$$\Phi''+Sc(f\Phi'-Kc\Phi^n)=0 \tag{8}$$

$$\left.\begin{array}{c} f(0)=S, f'(0)=\alpha+\gamma f''(0), \theta(0)=1, \Phi(0)=1, \\ f'(\infty)\to 0, \theta(\infty)\to 0, \Phi(\infty)\to 0 \end{array}\right\} \tag{9}$$

Here, $S>0, S=0, S<0$ represent suction, impermeable, and injection, respectively. Further, $\alpha>0$, $\alpha=0, and\ \alpha<0$ denote the stretching, rigid, and shrinking cases, respectively.

The friction coefficient (C_f), Nusselt number (Nu_x) and Sherwood number (Sh_x) are defined as:

$$C_f = \frac{\mu_{hnf}}{\rho_f u_w^2}\left(\frac{\partial u}{\partial y}\right)_{y=0} \Rightarrow Re_x^{1/2} C_f = \frac{\mu_{hnf}}{\mu_f} f''(0) \quad (10)$$

$$Nu_x = -\frac{k_{hnf} x}{k_f (T_w - T_\infty)}\left(\frac{\partial T}{\partial y}\right)_{y=0} \Rightarrow Re_x^{-1/2} Nu_x = -\frac{k_{hnf}}{k_f}\theta'(0) \quad (11)$$

$$Sh_x = -\frac{x}{(C_w - C_\infty)}\left(\frac{\partial C}{\partial y}\right)_{y=0} \Rightarrow Re_x^{-1/2} Sh_x = -\Phi'(0) \quad (12)$$

Here, shear stress $\tau_w = \mu_{hnf}\left(\frac{\partial u}{\partial y}\right)_{y=0}$, heat flux $q_w = -k_{hnf}\left(\frac{\partial T}{\partial y}\right)_{y=0}$, mass flux $q_m = -D_B\left(\frac{\partial C}{\partial y}\right)_{y=0}$ and $Re_x = u_w x/\nu_f$ is the local Reynolds number.

Here, ϕ_1 and ϕ_2 denote the volume fraction of $SWCNT$ and $MWCNT$, respectively. Moreover, $\phi_1 = \phi_2 = 0$ characterizes the regular fluid. Tables 1 and 2 represent the thermophysical properties of NF and HNF.

Table 1. Thermo-physical properties of NF and HNF.

Properties	NF	Hybrid NF
Density	$\rho_{nf} = (1-\phi_1)\rho_f + \phi_1\rho_{n1}$	$\rho_{hnf} = (1-\phi_2)\left[(1-\phi_1)\rho_f + \phi_1\rho_{n1}\right] + \phi_2\rho_{n2}$
Dynamic viscosity	$\mu_{nf} = \frac{\mu_f}{(1-\phi_1)^{2.5}}$	$\mu_{hnf} = \frac{\mu_f}{(1-\phi_1)^{2.5}(1-\phi_2)^{2.5}}$
Thermal conductivity	$\frac{k_{nf}}{k_f} = \frac{k_{n1} + 2k_f - 2\phi_1(k_f - k_{n1})}{k_{n1} + 2k_f + \phi_1(k_f - k_{n1})}$	$\frac{k_{hnf}}{k_{nf}} = \frac{k_{n2} + 2k_{nf} - 2\phi_2(k_{nf} - k_{n2})}{k_{n2} + 2k_{nf} + \phi_2(k_{nf} - k_{n2})}$
Heat capacity	$(\rho C_p)_{nf} = (1-\phi_1)(\rho C_p)_f + \phi_1(\rho C_p)_{n1}$	$(\rho C_p)_{hnf} = (1-\phi_2)\begin{bmatrix}(1-\phi_1)(\rho C_p)_f \\ +\phi_1(\rho C_p)_{n1}\end{bmatrix} + \phi_2(\rho C_p)_{n2}$
Electrical conductivity	$\frac{\sigma_{nf}}{\sigma_f} = 1 + \frac{3\left(\frac{\sigma_{n1}}{\sigma_f} - 1\right)\phi_1}{\frac{\sigma_{n1}}{\sigma_f} + 2 - \left(\frac{\sigma_{n1}}{\sigma_f} - 1\right)\phi_1}$	$\frac{\sigma_{hnf}}{\sigma_{nf}} = 1 + \frac{3\left(\frac{\sigma_{n2}}{\sigma_{nf}} - 1\right)\phi_2}{\frac{\sigma_{n2}}{\sigma_{nf}} + 2 - \left(\frac{\sigma_{n2}}{\sigma_{nf}} - 1\right)\phi_2}$

Table 2. Thermo-physical properties of water and NPs.

Properties	$\rho(kg/m^3)$	$C_p(J/kgK)$	$k(W/mK)$	$\sigma(\Omega^{-1}m^{-1})$
water	997	4179	0.613	0.05
$SWCNT$	2600	425	6600	4.8×10^7
$MWCNT$	1600	796	3000	3.3×10^6

3. Entropy Generation

The volumetric entropy generation rate is given as

$$E_G = \underbrace{\frac{k_{hnf}}{T_\infty^2}\left(\frac{\partial T}{\partial y}\right)^2}_{Thermal irreversibility} + \underbrace{\frac{(\sigma_{hnf} B_0^2)}{T_\infty}u^2}_{Joule dissipation irreversibility} + \underbrace{\frac{\mu_{hnf}}{T_\infty}\left(\frac{\partial u}{\partial y}\right)^2}_{Nanofluid friction irreversibility} + \underbrace{\frac{\mu_{hnf}}{T_\infty K p^*}u^2}_{Porosity irreversibility} + \underbrace{\frac{RD_B}{T_\infty}\left(\frac{\partial C}{\partial y}\frac{\partial T}{\partial y}\right) + \frac{RD_B}{C_\infty}\left(\frac{\partial C}{\partial y}\right)^2}_{Nanoparticle mass transfer irreversibility} \quad (13)$$

The entropy generation characteristic is $E_0 = \frac{a(T_w - T_\infty)k_f}{T_\infty \upsilon_f}$ and

$N_G = \frac{E_G}{E_0} = \frac{k_{hnf}}{k_f}A\theta'^2 + \frac{\sigma_{hnf}}{\sigma_f}MBrf'^2 + B\left[\phi'\theta' + \frac{A'}{A}\phi'^2\right] + \frac{\mu_{hnf}}{\mu_f}Br\left[\frac{f'}{Kp} + f''^2\right]$ is entropy-generation number

Here, $Br = \frac{\mu_f a^2 x^2}{k_f(T_w - T_\infty)}$ (Brinkman number), $B = \frac{RD_B}{k_f}(C_w - C_\infty)$ (Diffusion Parameter),$A = \frac{T_w - T_\infty}{T_\infty}$ and $A' = \frac{C_w - C_\infty}{C_\infty}$ (Temperature and Concentration difference parameter, respectively).

The Bejan number represents the fraction of mass and heat transport to the overall entropy.

$$Be = \frac{\frac{k_{hnf}}{k_f}A\theta'^2 + B\left[\phi'\theta' + \frac{A'}{A}\phi'^2\right]}{\frac{k_{hnf}}{k_f}A\theta'^2 + \frac{\sigma_{hnf}}{\sigma_f}MBrf'^2 + B\left[\phi'\theta' + \frac{A'}{A}\phi'^2\right] + \frac{\mu_{hnf}}{\mu_f}Br\left[\frac{f'}{Kp} + f''^2\right]} \quad (14)$$

From equation (11), it is evident that the Bejan number (Be) is in the range between 0 and 1. It is implied that heat transmission predominates over irreversibility when $Be >> 0.5$ the irreversibility is brought on by thermal radiation, viscous dissipation, and Joule-heating $Be << 0.5$. This suggests that irreversibility resulting from heat transfer through thermal radiation, Joule heating, and viscous dissipation is similar when *Be* = 0.5.

4. Numerical Solution and Validation of the Study

The numerical solution is obtained for the system of non-linear ODEs (7) – (9), applying MATLAB 2024a software with the bvp4c code for the step size 10^{-2} and error tolerance10^{-5}. The computational procedure is illustrated through the flow chart in Figure 2. Further, to validate the numerical code, the present results have been validated with the previously published findings [11, 16,17], as presented in Table 3.

In this technique, the boundary value problem (BVP) converts into a system of first-order IVPs and is given by:

$$f' = p$$

$$p' = q$$

$$q' = \frac{\frac{\rho_{hnf}}{\rho_f}}{\frac{\mu_{hnf}}{\mu_f}}\left[-fq + p^2 + \frac{\frac{\sigma_{hnf}}{\sigma_f}}{\frac{\rho_{hnf}}{\rho_f}}Mp + \frac{\frac{\mu_{hnf}}{\mu_f}}{\frac{\rho_{hnf}}{\rho_f}Kp}p\right] \quad (15)$$

$$\theta' = s$$

$$s' = -Pr\frac{k_f}{k_{hnf}}\left\{-\frac{(\rho C_p)_f}{(\rho C_p)_{hnf}}fs - \frac{\sigma_{hnf}}{\sigma_f}MEcp^2 - \frac{\mu_{hnf}}{\mu_f}Ecq^2\right\} \quad (16)$$

$$\Phi' = w$$

$$w' = -Sc[fw - Kc\Phi^n] \quad (17)$$

$$f(0) = S, p(0) = \alpha + \gamma q(0), s(0) = 1, \Phi(0) = 1$$

$$p(\infty) \to 0, \theta(\infty) \to 0, \Phi(\infty) \to 0 \quad (18)$$

Table 3. Comparison of $-\theta'(0)$ for *Pr* when $M = Ec = Sc = \gamma = 0$ and $\lambda_1 = 1$.

Pr	Khan and Pop [11]	Ahmad *et al.* [16]	Devi and Devi [17]	Present study
2	0.9113	0.91045	0.91135	0.911353
7	1.8954	1.89083	1.89540	1.895409
20	3.3539	3.35271	3.35390	3.353940
70	6.4621	6.47814	----	6.462262

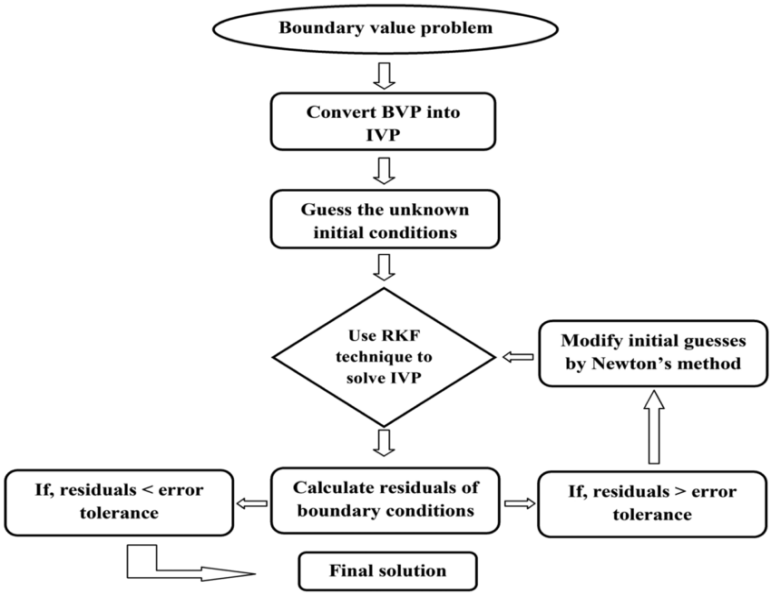

Figure 2. Flow chart of solution procedure.

5. Results and Discussion

In the velocity distribution, instability in inviscid flow primarily depends on the presence of an inflection point. In real fluids, however, stability is mainly governed by viscosity rather than by the presence of inflection points. For velocity profiles involving a fluid bounded by solid surfaces, viscosity generally has a destabilizing influence. In contrast, the present model of nanofluid and hybrid nanofluid counteracts this effect of viscosity, leading to a stabilizing behavior. As a result, no inflection point or flow reversal is observed in any of the velocity profiles.

Figure 3 reveals the following notable findings. Curves I and II show that an increase in ϕ_1, the volume fraction of $SWCNT$ increases the velocity in the absence of ϕ_2 (MWCNT). Curve III shows the presence of ϕ_2, combined with ϕ_1, enhances the velocity substantially. Curves III and IV show that Loterntz force, a resistive force, decreases the velocity due to the interaction of the applied magnetic field with electrically conducting fluid in motion. Curves IV and V show that the effect is significant, with an increase in the permeability parameter leading to a substantial decrease in velocity across the entire flow domain. This is due to the ease of fluid flow. The higher value of Kp tends to free flow, i.e., $Kp \to \infty$. The case without a porous medium. Consequently, the velocity attains the ambient state. This is evident from Curve VI.

Figure 4 displays the effects of two important parameters, i.e., α (stretching) and γ (slip). It is observed that an increase in the slip parameter reduces the velocity, thereby accelerating the attainment of the ambient state. The physical interpretation runs as follows: The shearing stress between the solid boundary and fluid layer decreases. From equation (9), it is seen that if $\alpha = 0$, there is no stretching at the boundary. The non-zero value of α, contributes to the primary velocity $f'(0)$ at the boundary, which leads to a higher start-up velocity at the bounding surface. Hence, the fall will be quicker to attend the ambient state, which is what is shown in Figure 4.

Figure 5 shows the effect of suction $(S > 0)$ and injection $(S < 0)$ parameter on the velocity distribution in the presence of nanofluid and hybrid nanofluid, and the porosity parameter. The suction parameter $(S > 0)$ declines the velocity distribution by thinning the

boundary layer, whereas the injection parameter $(S < 0)$ enhances velocity due to fluid blowing at the surface. It is quite natural, as the fluid mass increases in the flow domain, slowing down the momentum transport, whereas for suction, as $|S|$ increases the velocity decreases due to faster momentum transport.

Figure 6 is quite important as it is related to two volume fractions characterizing HNF (ϕ_2) and NF (ϕ_1). It is observed that as ϕ_2 increases, the temperature in the flow domain increases at each and every point, which corroborates the efficiency of HNF over NF. An increase in the volume fraction of nanoparticles in a hybrid nanofluid enhances the temperature distribution, as the improved effective thermal conductivity facilitates greater heat absorption and retention within the boundary layer. A significant remark is that the combined effect of ϕ_1 and ϕ_2 escalates the thermal energy considerably; consequently, the temperature of the flow domain increases, which is what is expected from the present model.

Figure 7 depicts a noteworthy outcome on thermal energy transfer with a symmetric variation about the line joining (0,1) and (2,0). Suction $(S > 0)$ reduces the thermal boundary layer thickness by drawing fluid particles toward the surface, which enhances heat transfer and results in a lower temperature profile near the boundary. On the other hand, injection $(S < 0)$ supplies additional fluid into the boundary layer, thickening the thermal boundary layer and raising the temperature distribution. Thus, suction has a stabilizing and cooling effect, whereas injection tends to destabilize the flow and elevate the temperature profile. Thus, in the present flow model, suction $(S > 0)$ and injection $(S < 0)$ play useful phenomena serving as surface heating/cooling in a heat exchanger very efficiently. It is a noteworthy contribution of the HNF and NF system.

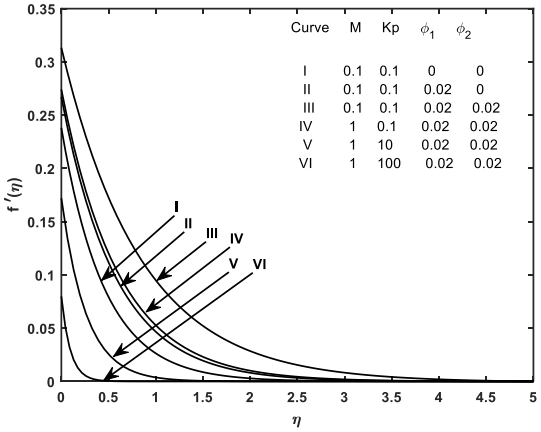

Figure 3. Velocity profiles versus M *and* Kp when $n = S = 2, Ec = 0.1, Pr = 6.2, Sc = 2, Kc = 0.1, \alpha = \gamma = 0.5$.

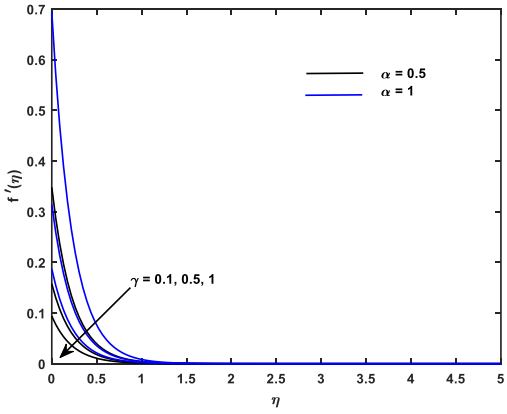

Figure 4. Velocity profiles versus α and γ when $\phi_1 = \phi_2 = 0.02, Kp = 10, n = S = Sc = 2, Ec = 0.1, Pr = 6.2,\ Kc = 0.1, M = 0.5$.

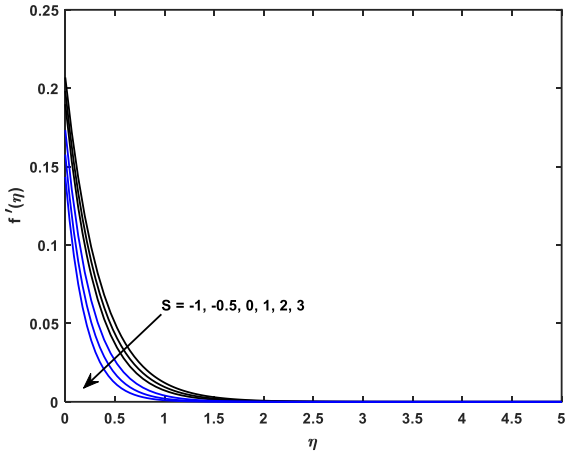

Figure 5. Velocity profiles versus S when $\phi_1 = \phi_2 = 0.02, Kp = 10, n = Sc = 2, Ec = 0.1, Pr = 6.2,\ Kc = 0.1, \alpha = \gamma = M = 0.5$.

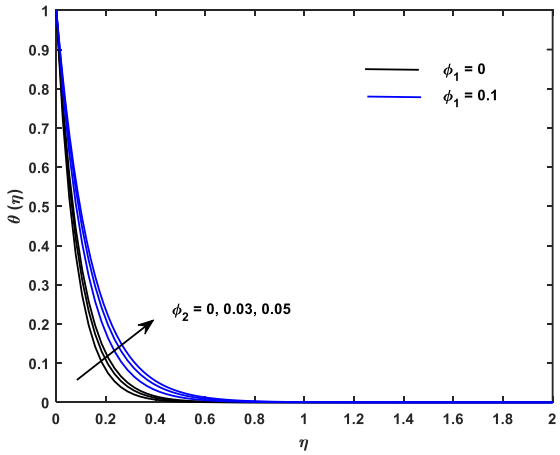

Figure 6. Temperature profiles versus ϕ_1 and ϕ_2 when $Kp = 10, n = S = Sc = 2, Ec = 0.1, Pr = 6.2, S = 2, Kc = 0.1, \alpha = \gamma = M = 0.5$.

Figure 8 shows the effect of Eckert number, a measure of the dissipation effects on the HNF and NF flow. It presents a quantitative increase in temperature for a higher value of Ec. Thus, it is suggested that the parameter Ec be assigned the value as per the design requirement to increase the dissipation of the thermal energy from the fluid mass.

Figure 9 depicts the effect of an important parameter related to solutal concentration (thermo-diffusion), i.e., Schmidt number (ratio of kinematic viscosity and mass diffusion). The Prandtl number and Schmidt number are quite analogous to thermal diffusion and solutal diffusion (i.e., heat and mass transfer). It is seen that an increase in Sc decreases the solutal concentration. It is well established that a heavier species reduces the concentration. It is further seen that an increase in order in chemical reaction (n) does not contribute much to mass transfer processes in the present model.

Figure 10 depicts the effects of the chemical reaction rate coefficient ($Kc < 0$, constructive and $Kc > 0$, destructive) in the presence of the combined effects of ϕ_1 and ϕ_2 in the presence of a magnetic field but in a relatively high permeability medium ($Kp = 10$) and low thermal conductivity ($Pr = 6.2$) on the concentration distribution. It is seen that an increase in the first-order destructive chemical reaction ($Kc > 0$), the concentration profiles $\Phi(\eta)$ decrease; the inference is quite trivial, but for constructive reaction ($Kc < 0$), $|Kc|$ increases the solutal concentration of the flow domain.

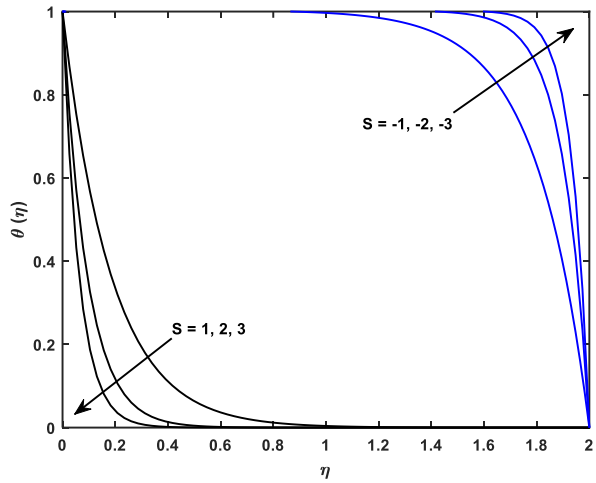

Figure 7. Temperature profiles versus S when $\phi_1 = \phi_2 = 0.02, Kp = 10, n = Sc = 2, Ec = 0.1, Pr = 6.2, Kc = 0.1, \alpha = \gamma = M = 0.5$.

Table 4 indicates the skin friction coefficient (C_f) at the bounding surface. It remains negative throughout for all the parameters, whereas the Nusselt number (Nu_x) and Sherwood number (Sh_x) remain positive. The increase in skin friction for the increase in parameters indicates the progressive thinning of the boundary layer. For the Nusselt number $(-\theta'(0) > 0)$, the heat flux for the tabulated values shows heat flows from the plate to the fluid, analogous to $T_W > T_\infty$ and $Ec = 0$. Reversely, $-\theta'(0) < 0$, heat flows from the fluid to the plate. In the presence of thermal dissipation $(Ec \neq 0)$ the reverse may happen even if $T_W > T_\infty$. The variation of the Sherwood number is analogous to heat transfer. Detailed analysis of the tabulated values in Table 4 reveals the following:

An increase in the stretching parameter (α) increases the skin friction, but the slip parameter (γ) decreases. The slip occurs in thin liquids. Therefore, those who experience less shearing stress at the plate. It is further seen that both constructive and destructive chemical reaction parameters increase the Sherwood number. This may be a contribution of a hybrid nanofluid. Moreover, an increase in permeability parameter Kp, increases the $|C_f|$. Also, higher values of the injection parameter $(S > 0)$ leads to higher values of $|C_f|$, but in the case of suction $(S < 0)$ the reverse effect is observed. Hence, the suction reduces the boundary layer thickness, which is a desirable outcome. The tabulated values of Nu_x and Sh_x are both positive for all the parameters. The first order slip increases the rate of heat (Nu_x), but it decreases the mass transfer coefficient (Sh_x). The effect of the stretching parameter (α) is opposite to that of the slip parameter (γ). The effect of injection is to decrease both the coefficients, i.e., heat and mass at the bounding surface, resulting in cooling of the plate with low mass flux, but the suction does the reverse. Therefore, suction as well as injection at the bounding surface are to be adjusted as per the design requirement.

Quantitative Analysis: As Kp decreases from 100 to 1, the skin friction coefficient (C_f) increases from −0.579868 to −0.222835, i.e., gives rise to a decrease in $|C_f|$ 61.57%, indicating reduced resistive drag due to enhanced permeability of the medium. Meanwhile, the Nusselt number increases by about 0.21%, while the Sherwood number increases by nearly 0.20%, indicating marginal improvements in heat and mass transfer, respectively.

For higher values of α, the skin friction coefficient shows a significant increase of 106.37% in magnitude (−1.146101 at $\alpha = 0.5$, −2.365287 at $\alpha = 1$). However, Nu_x decreases

from 12.076354 to 11.793856), showing reduced heat transfer rates. In contrast, Sh_x increases from 10.178261 to 10.321217, which suggests stronger concentration diffusion effects.

Increasing Kc has a strong influence on Sh_x. Increasing Kc from -0.5 to 0.5 increases Sh_x by about 3.76%, showing a noticeable positive influence. A positive Kc (generative reaction) enhances concentration transfer, whereas a negative Kc (destructive reaction) suppresses it. The Nusselt number, however, remains unchanged, indicating that chemical reactions predominantly affect mass transfer rather than heat transfer.

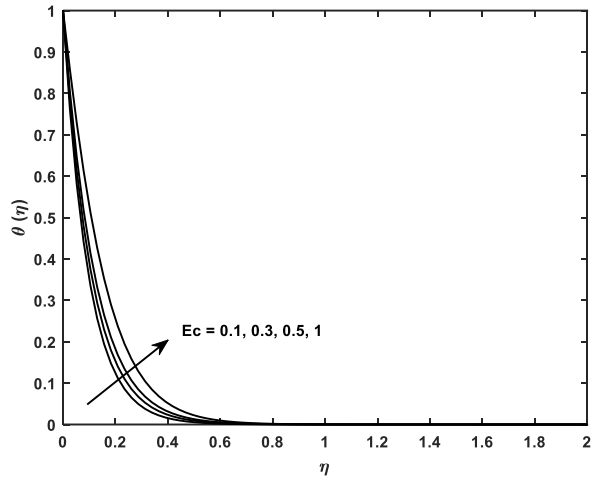

Figure 8. Temperature profiles versus Ec when $\phi_1 = \phi_2 = 0.02, Kp = 10, n = S = Sc = 2\ Pr = 6.2, Kc = 0.1, \alpha = \gamma = M = 0.5$.

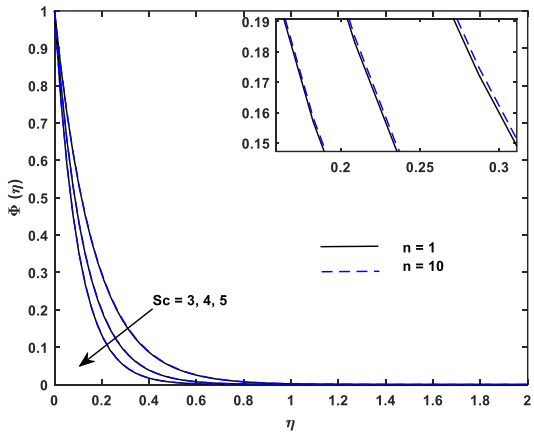

Figure 9. Concentration profiles versus Sc and n when $\phi_1 = \phi_2 = 0.02, Kp = 10, S = 2, Ec = 0.1, Pr = 6.2, Kc = 0.1, \alpha = \gamma = M = 0.5$.

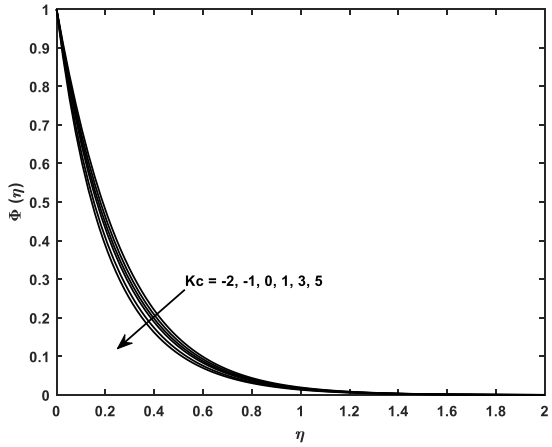

Figure 10. Concentration profiles versus γ when $\phi_1 = \phi_2 = 0.02, Kp = 10, S = n = Sc = 2, Ec = 0.1, Pr = 6.2, \alpha = \gamma = M = 0.5$.

When the suction parameter $(S > 0)$ decreases from $S = 2$ to 1, the skin friction increases from -0.797299 to -0.726896, while both Nu_x and Sh_x drop significantly (from 11.806797 to 5.868214 and 10.23 to 5.459269). For injection $(S = -1)$, Nu_x and Sh_x are drastically reduced (to negative or near-zero values), implying a sudden fall of heat and mass transfer performance due to fluid blowing at the boundary.

Table 4. Computational values of C_f, Nu_x and Sh_x when $\phi_1 = \phi_2 = 0.05, M = 0.5, Pr = 6.2, n = 2$ and $Sc = 5$.

Kp	α	γ	Ec	Kc	S	C_f	Nu_x	Sh_x
100	0.1	0.1	0.1	0.1	2	-0.579868	12.053831	10.036225
10						-0.334243	12.069716	10.049137
1						-0.222835	12.079507	10.056557
	0.5					-1.146101	12.076354	10.178261
	1					-2.365287	11.793856	10.321217
		0.5				-1.255496	12.063261	10.191828
		1				-0.797299	12.100697	10.133871
			0.3			-0.797299	11.953747	10.133871
			0.5			-0.797299	11.806797	10.133871
				0.5		-0.797299	11.806797	10.230931
				1		-0.797299	11.806797	10.350577
				0		-0.797299	11.806797	10.109414
				-0.3		-0.797299	11.806797	10.035570
				-0.5		-0.797299	11.806797	9.860421
				-1		-0.797299	11.806797	9.860421
				0.5	1	-0.726896	5.868214	5.459269
					0	-0.644021	0.649029	1.563393
					-1	-0.559015	-0.184619	0.4551424
					-2	-0.482658	-0.100835	0.244443

6. Conclusions

A noteworthy finding of the present flow model is that the presence of both volume fractions of hybrid nanofluid and nanofluid $(\phi_1 = \phi_2 = 0.02)$ accelerates the velocity with a low magnetic parameter as well as the permeability of the medium. This outcome is beneficial to transport processes in the industrial application, energizing the flow setup.

Both suction and injection at the surface are useful for attaining the ambient state, which reduces the molar concentration.

The higher value of thermal dissipation (Ec) increases the temperature in the fluid.

The heavier diffusing species decreases the concentration profiles.

Higher values of the injection parameter $(S > 0)$ leads to higher values of $|C_f|$ but in the case of suction $(S < 0)$ the reverse effect is observed. Hence, the suction reduces the boundary layer thickness, which is a desirable outcome.

Increasing Kc from -0.5 to 0.5 increases Sh_x by about 3.76%**,** showing a noticeable positive influence.

Decrease in porosity parameter. (Kp) from 100 to 1 gives rise to a decrease in skin friction coefficient (C_f) 61.57% and the Nusselt number increases by about 0.21%, while the Sherwood number increases by nearly 0.20%, indicating marginal improvements in heat and mass transfer, respectively.

7. Future Scope

The present study can be extended in several directions to increase its applicability. Future work may consider unsteady and three-dimensional stretching surfaces, which are more representative of real-world industrial processes. Incorporating thermal radiation and variable

fluid properties would enhance the model's relevance for energy storage and geophysical flows. Further, the present model can be extended to non-Newtonian fluids, such as Casson, Powell–Eyring, Phan–Thien–Tanner, or Carreau fluids, which could capture complex flow behaviors. Additionally, experimental validation of the numerical results and optimization studies using entropy-generation minimization techniques would provide valuable insights into the design of advanced cooling, catalytic, and microfluidic devices.

Author Contributions

Conceptualization, P.P., H.I. and K.S.; methodology, P.P., H.I. and K.S.; software, K.S.; validation, H.I. and K.S.; formal analysis, P.P., H.I. and K.S.; investigation, P.P., H.I. and K.S.; resources, P.P., H.I. and K.S.; data curation, P.P., H.I. and K.S.; writing—original draft preparation, P.P., H.I. and K.S.; writing—review and editing, K.S.; visualization, H.I. and K.S.; supervision, H.I. and K.S. All authors have read and agreed to the published version of the manuscript.

Institutional Review Board Statement

Not applicable.

Informed Consent Statement

Not applicable.

Data Availability Statement

Data supporting the findings of this study are available upon reasonable request from the corresponding author.

Funding

This research received no external funding.

Acknowledgments

The authors thank Prof. G. C. Dash for his valuable suggestions and timely help in improving the quality of the paper.

Conflicts of Interest

The authors declare no conflict of interest.

Abbreviations

The following abbreviations are used in this manuscript:

Abbreviation	Definition
NF	Nanofluid
HNF	Hybrid Nanofluid
NP	Nanoparticle
MHD	Magnetohydrodynamic
2D	Two Dimensional
ODE	Ordinary Differential Equation

PDE	Partial Differential Equations
BVP	Boundary Value Problem
IVP	Initial Value Problem
SWCNT	Single-Walled Carbon Nanotube
MWCNT	Multi-Walled Carbon Nanotube
CNT	Carbon Nanotube
x,y	Cartesian Coordinate System (m)
u,v	Velocity Components Along
x,y	Directions Respectively (m/s)
B_0	Magnetic field strength
T	Temperature
T_w	Temperature at the Sheet
T_∞	Ambient Temperature
k_{hnf}	Thermal Conductivity of Hybrid Nanofluid (m^2/s)
k_f	Thermal Conductivity of Base Fluid (m^2/s)
$Pr\left(=\frac{(\mu C_p)_f}{k_f}\right)$	Prandtl number
k_{nf}	Thermal Conductivity of Nanofluid (m^2/s)
D_B	Brownian Motion Coefficient (m^2/s)
S	Suction/Injection Parameter
$v_0 v_0$	Suction Velocity
n	Rate of Chemical Reaction
$Ec\left(=\frac{u_w^2}{(C_p)_f (T_w - T_\infty)}\right)$	Eckert Number
$M\left(=\frac{\sigma_f B_0^2}{a\rho_f}\right)$	Magnetic Parameter
C_f	Local Skin Friction Coefficient
$Sc\left(=\frac{\nu_f}{D_B}\right)$	Schmidt Number
Kc^*	Rate of Chemical Reaction
$Kc\left(=\frac{Kc^*}{a}\right)$	Chemical Reaction Parameter
Kp^*	Permeability of the Porous Medium
$Kp\left(=\frac{aKp^*}{\nu_f}\right)$	Porosity Parameter
f	Dimensionless Velocity
Nu_x	Local Nusselt Number
Re_x	Local Reynolds number
α	Stretching Parameter
β	Slip Constant
$\gamma\left(=\beta\sqrt{\frac{a}{\nu_f}}\right)$	Velocity Slip Parameter
ψ	Stream Function
θ	Dimensionless Temperature
Φ	Dimensionless Nanoparticle Volume Fraction
ν_{hnf}	Kinetic Velocity of Hybrid Nanofluid (m^2/s)
ν_f	Kinetic Velocity of Base Fluid (m^2/s)
σ_{hnf}	Electrical Conductivity of Hybrid Nanofluid (Ω^{-1} m^{-1})
σ_{nf}	Electrical Conductivity of Nanofluid (Ω^{-1} m^{-1})
ρ_{hnf}	Density of Hybrid Nanofluid (kg/m^3)
ρ_{nf}	Density of Nanofluid (kg/m^3)
ρ_f	Density of Base Fluid (kg/m^3)
μ_{hnf}	Viscosity of Hybrid Nanofluid (kg/m s)
μ_{nf}	Viscosity of Nanofluid (kg/m s)
$(\rho C_p)_{hnf}$	Heat Capacitance of Hybrid Nanofluid (J/kg K)
$(\rho C_p)_{nf}$	Heat Capacitance of Hybrid Nanofluid (J/kg K)

References

1. Sakiadis, B.C. Boundary-layer behavior on continuous solid surfaces: II. The boundary layer on a continuous flat surface. *AIChE J.* **1961**, *7*, 221–225, https://doi.org/10.1002/aic.690070211.
2. Crane, L.J. Flow past a stretching plate. *Z. Angew. Math. Phys.* **1970**, *21*, 645–647, https://doi.org/10.1007/BF01587695.
3. Choi, S.U.; Eastman, J.A. Enhancing thermal conductivity of fluids with nanoparticles. *ASME-Publ.-Fed.* **1995**, *231*, 99–106.
4. Buonigiorno, J. Convective transport in nanofluids. *J. Heat Transf.* **2010**, *128*, 240–250, https://doi.org/10.1115/1.2150834.
5. Nadeem, S.; Haq, R.U.; Akbar, N.S. MHD three-dimensional boundary layer flow of Casson nanofluid past a linearly stretching sheet with convective boundary condition. *IEEE Transactions on Nanotechnology*. **2014**, *13*, 109-115, http://dx.doi.org/10.1109/TNANO.2013.2293735.
6. Mustafa, M.; Khan, J.A.; Hayat, T.; Alsaedi, A. Buoyancy effects on the MHD nanofluid flow past a vertical surface with chemical reaction and activation energy, *International Journal of Heat and Mass Transfer*. **2017**, 108, 1340-1346, https://doi.org/10.1016/j.ijheatmasstransfer.2017.01.029.
7. Rao, S.; Deka, P.N. Numerical Analysis of MHD Hybrid Nanofluid Flow a Porous Stretching Sheet with Thermal Radiation. *Int. J. Appl. Comput. Math*. **2024**, 10, 95, https://doi.org/10.1007/s40819-024-01734-4
8. Rashidi, M.M.; Abelman, S.; Mehr, N.H. Entropy generation in steady MHD flow due to a rotating porous disk in a nanofluid. *Int. J. Heat Mass Transf.* **2013**, *62*, 515–525, https://doi.org/10.1016/j.ijheatmasstransfer.2013.03.004.
9. Zahor, R.; Tufail, M.; Javaid, S.; Shehzad, S.A. Modeling entropy generation of magnetohydrodynamics flow of nanofluid in a porous medium: A review. *Int. J. Numer. Methods Heat Fluid Flow.* **2023**, *33*, 751–771, https://doi.org/10.1108/HFF-05-2022-0266.
10. Elhaj, M.A.; Imtiaz, S.A.; Naterer, G.F.; Zendehboudi, S. Entropy generation minimization of two-phase flow irreversibilities in hydrocarbon reservoirs. *Energies* **2023**, *16*, 4096. https://doi.org/10.3390/en16104096.
11. Khan, W.A.; Pop, I. Boundary-layer flow of a nanofluid past a stretching sheet. *International Journal of Heat Mass Transfer* **2010**, *53*, 2477–2483, https://doi.org/10.1016/j.ijheatmasstransfer.2010.01.032.
12. Swain, K.; Animasaun, I.L.; Ibrahim, S.M. Influence of exponential space-based heat source and Joule heating on nanofluid flow over an elongating/shrinking sheet with an inclined magnetic field. *Int. J. Ambient Energy* **2021**, *43*, 4045–4057, https://doi.org/10.1080/01430750.2021.1873854.
13. Al-Kouz, W.; Swain, K.; Mahanthesh, B.; Jamshed, W. Significance of exponential space-based heat source and inclined magnetic field on heat transfer of hybrid nanoliquid with homogeneous-heterogeneous chemical reactions. *Heat Transfer* **2021**, *50*, 4086–4102, https://doi.org/10.1002/htj.22065.
14. Swain, K.; Oudina, F.M.; Abo-Dahab, S.M. Influence of MWCNT/Fe_3O_4 hybrid nanoparticles on an exponentially porous shrinking sheet with chemical reaction and slip boundary conditions. *J. Therm. Anal. Calorim.* **2022**, *147*, 1561–1570, https://doi.org/10.1007/s10973-020-10432-4.
15. Waini, I.; Ishak, A.; Pop, I. Hybrid nanofluid flow over a permeable non-isothermal shrinking surface. *Mathematics* **2021**, *9*, 538, https://doi.org/10.3390/math9050538.
16. Ahmad, S.; Ali, K.; Rizwan, W.; Ashraf, M. Heat and mass transfer attributes of copper-aluminum oxide hybrid nanoparticles flow through a porous medium. *Case Stud. Therm. Eng.* **2021**, *25*, 100932, https://doi.org/10.1016/j.csite.2021.100932.
17. Devi, S.P.A.; Devi, S.S.U. Numerical investigation of hydromagnetic hybrid Cu-Al_2O_3/water nanofluid flow over a permeable stretching sheet with suction. *Int. J. Nonlinear Sci. Numer. Simul.* **2016**, *17*, 249–257, https://doi.org/10.1515/ijnsns-2016-0037.
18. Triveni, K.; Mahanthesh, B. Heat transport of hybrid nanomaterial in an annulus with quadratic Boussinesq approximation. *Appl. Math. Mech.* **2021**, *42*, 885–900, https://doi.org/10.1007/s10483-021-2739-6.
19. Mebarek-Oudina, F.; Dharmaiah, G.; Rama Prasad, J.L.; Vaidya, H.; Kumari, M.A. Thermal and flow dynamics of magnetohydrodynamic Burgers' fluid induced by a stretching cylinder with internal heat generation and absorption. *Int. J. Thermophys.* **2025**, *25*, 100986, https://doi.org/10.1016/j.ijft.2024.100986.
20. Raza, J.; Mebarek-Oudina, F.; Ali, H.; Sarris, I.E. Slip effects on Casson nanofluid over a stretching sheet with activation energy: RSM analysis. *Front. Heat Mass Transf.* **2024**, *22*, 1017–1041, https://doi.org/10.32604/fhmt.2024.052749.

21. Swain, K.; Mahanthesh, B. Thermal Enhancement of Radiating Magneto-Nanoliquid with Nanoparticles Aggregation and Joule Heating: A Three-Dimensional Flow. *Arab. J. Sci. Eng.* **2021**, *46*, 5865–73, https://doi.org/10.1007/s13369-020-04979-5.
22. Anil Kumar, M.; Mebarek-Oudina, F.; Mangathai, P.; Shah, N.A.; Vijayabhaskar, Ch.; Venkatesh, N.; Fouad, Y. The impact of Soret Dufour and radiation on the laminar flow of a rotating liquid past a porous plate via chemical reaction. *Mod. Phys. Lett. B* **2025**, *39*, 2450458, https://doi.org/10.1142/S021798492450458X.
23. Zainal, N.A.; Nazar, R.; Naganthran, K.; Pop. I. The Impact of Thermal Radiation on Maxwell Hybrid Nanofluids in the Stagnation Region. *Nanomaterials* **2022**, *12*, 1109, https://doi.org/10.3390/nano12071109.
24. Sankar Reddy, T.; Roja, P.; Ibrahim, S.M.; Lorenzini. G. Thermal Radiation and Viscous Dissipation Effects on (MHD) Bioconvection Stream of Maxwell Nanoliquid Over a Permeable Vertical Plate Due to Gyrotactic Microorganisms. *Math. Model. Eng. Probl.* **2022**, *9*, 325–35, https://doi.org/10.18280/mmep.090205.
25. Waseem, F.; Sohail, M.; Singh, A. Entropy Analysis of Three-dimensional Stretched Magnetized Hybrid Nanofluid with Thermal Radiation and Heat Generation. *BioNanoSci.* **2024**, *14*, 547–565, https://doi.org/10.1007/s12668-023-01267-y.
26. Ould Said, B.; Mebarek-Oudina, F.; Medebber, M.A. Magneto-hydro-convective nanofluid flow in porous square enclosure. *Front. Heat Mass Transf.* **2024**, *22*, 1343–1360, https://doi.org/10.32604/fhmt.2024.054164.
27. Mebarek-Oudina, F.; Bouselsal, M.; Biswas, N.; Vaidya, H.; Ramesh, K. Heat transfer in a zigzag wall cavity and different obstacles filled with MgO-SWCNT/water hybrid nanofluids. *Mod. Phys. Lett. B* **2025**, *39*, 2550163, https://doi.org/10.1142/S0217984925501635.
28. Aarathi, T.; Subramanyam Reddy, A.; Jagadeshkumar, K.; Ramachandra Prasad, V.; Bég, O.A. Entropy generation in a chemically reactive magnetohydrodynamic unsteady micropolar nanofluid flow with activation energy over an inclined stretching sheet: A Buongiorno model approach. *Proc. Inst. Mech. Eng. E: J. Process Mech. Eng.* **2026**, *240*, 2044-2060, https://doi.org/10.1177/09544089241272900.
29. Barik, A.K.; Rout, S.; Senapati, J.R.; Awad, M.M. Effects of velocity, thermal and concentration slips on the entropy generation of nanofluid over an inclined sheet. *Int. J. Numer. Methods Heat Fluid Flow* **2024**, *34*, 1117–1148, https://doi.org/10.1108/HFF-08-2023-0449.
30. Kumar, M.; Kumar, N.N.; Mondal, P.K. Irreversibility analysis of hydromagnetic viscoelastic Ag-Al_2O_3/water hybrid nanofluid over a stretching sheet. *Proc. Inst. Mech. Eng. C: J. Mech. Eng. Sci.* **2023**, *239*, 1230–1245, https://doi.org/10.1177/09544089231193586.
31. Naseem, T.; Mebarek-Oudina, F.; Vaidya, H.; Bibi, N.; Ramesh, K.; Khan, S.U. Numerical analysis of entropy generation in Joule heated radiative viscous fluid flow over a permeable radially stretching disk. *CMES - Comput. Model. Eng. Sci.*. **2025**, *143*, 351–371, https://doi.org/10.32604/cmes.2025.063196.
32. Mahboobtosi, M.; Hosseinzadeh, K.; Najafpour, A.; Ganji, D.D. Entropy generation analysis of kerosene oil flow with ternary hybrid nanoparticles on the stretchable exponential surface. *Int. J. Model. Simul.* **2024**, *8*, pp. 1–15. https://doi.org/10.1080/02286203.2024.2349506.
33. Samantaray, S.S.; Misra, A.; Shaw, S.; Nayak, M.K.; Nazari, S.; Boukhris, I.; Chamkha, A.J. Recent advances on entropy analysis of composite nanofluids—A critical review. *Results Eng.* **2024**, *22*, 101980, https://doi.org/10.1016/j.rineng.2024.101980.
34. Lone, S.A.; Raizah, Z.; Alrabaiah, H.; Shahab, S.; Saeed, A.; Khan, A. Exploring convective conditions in three-dimensional rotating ternary hybrid nanofluid flow over an extending sheet: A numerical analysis. *J. Therm. Anal. Calorim.* **2024**, 150, 2651-2666, https://doi.org/10.1007/s10973-024-13070-2.
35. Mahabaleshwar, U.S.; Rudraiah, M.; Huang, H.; Sunden, B.A. An impact of ternary nanofluid on a micropolar fluid with inclined MHD, slip flow and heat transfer. *Int. J. Numer. Methods Heat Fluid Flow* **2024**, *34*, 2065–2093, https://doi.org/10.1108/HFF-07-2023-0384.
36. Kumar, A.; Sharma, B.K.; Sharma, M.; Almohsen, B.; Sarris, I.E. Entropy Generation Optimization for Casson Hybrid Nanofluid Flow Along a Curved Surface With Bioconvection Mechanism and Exothermic/Endothermic Catalytic Reaction. *Adv. Theory Simul.* **2025**, *8*, 2401554, https://doi.org/10.1002/adts.202401554.

Publisher's Note & Disclaimer